

## Surface susceptibility and conductivity of MoS<sub>2</sub> and WSe<sub>2</sub> monolayers: A first-principles and ellipsometry characterization

Joshua D. Elliott<sup>1,2,\*</sup>, Zhemi Xu<sup>1,†</sup>, Paolo Umari<sup>1,2</sup>, Gaurav Jayaswal<sup>3</sup>, Mingguang Chen<sup>4</sup>, Xixiang Zhang<sup>4</sup>,  
Alessandro Martucci<sup>5</sup>, Margherita Marsili<sup>6</sup>, and Michele Merano<sup>1</sup>

<sup>1</sup>*Dipartimento di Fisica e Astronomia “Galileo Galilei”, Univeristà degli Studi di Padova, via Marzolo 8, I-35131, Padova Italy*


<sup>2</sup>*CNR-IOM DEMOCRITOS, Consiglio Nazionale delle Ricerche–Istituto Officina dei Materiali, c/o SISSA,  
Via Bonomea 265, 34136, Trieste, Italy*

<sup>3</sup>*King Abdullah University of Science and Technology, Computer, Electrical, and Mathematical Sciences and Engineering Division,  
Thuwal 23955-6900, Saudi Arabia*

<sup>4</sup>*King Abdullah University of Science and Technology, Physical Science and Engineering, Thuwal 23955-6900, Saudi Arabia*

<sup>5</sup>*Dipartimento di Ingegneria Industriale, Università degli studi di Padova, via Marzolo 9, 35131 Padova, Italy*

<sup>6</sup>*Laboratoire des Solides Irradiés, École Polytechnique, CNRS F-91128 Palaiseau, France*

 (Received 19 April 2019; revised manuscript received 26 September 2019; published 13 January 2020)

We employ a recent formulation for the optical properties of two-dimensional crystals from first principles [L. Matthes *et al.*, *New J. Phys.* **16**, 105007 (2014); L. Matthes *et al.*, *Phys. Rev. B* **94**, 205408 (2016)] to compute the surface susceptibility and surface conductivity of MoS<sub>2</sub> and WSe<sub>2</sub> monolayers [G. Jayaswal *et al.*, *Opt. Lett.* **43**, 703 (2018)]. As electron-hole interactions are known to be crucial for the description of the absorption spectrum of monolayer transition metal dichalcogenides, the excitonic dielectric function is computed at the Bethe-Salpeter equation level, including spin-orbit interactions. For both of these examples, excellent agreement with experimental ellipsometry measurements is obtained. Driven by the emergence of additional features in our theoretical results, we applied a second-derivative analysis in order to identify excited exciton peaks in the ellipsometric spectra.

DOI: [10.1103/PhysRevB.101.045414](https://doi.org/10.1103/PhysRevB.101.045414)

### I. INTRODUCTION

Monolayer (ML) transition metal dichalcogenides (TMDCs) are among some of the most well documented two-dimensional (2D) materials in the post graphene era [1–4]. They are single layered sheets comprised of covalently bonded MX<sub>2</sub> moieties, where M denotes a transition metal and X one the chalcogens S, Se, or Te. Particularly intense interest in TMDCs has been stimulated by favorable electronic properties, which arise due to quantum confinement effects in the monolayer limit.

A large amount of attention has focused on the prototypical monolayer MoS<sub>2</sub> [5–16], whose band structure has a direct gap in the visible range of the electromagnetic spectrum [5,8], yet a direct gap is also confirmed for MoSe<sub>2</sub> and WS<sub>2</sub> [17]. The crossover from indirect-gap materials in the bulk phase to single-layer direct-gap materials is accompanied by improved optical absorption, strong photoluminescence, and large exciton and trion-exciton binding energies [5,6,9,18]. These exciting properties have prompted applications in diverse fields [2], for example as field effect transistors [19,20], logic circuits [21,22], and phototransistors [23–25].

First-principles simulations are a popular tool that can be used to further elucidate the behavior of monolayer TMDCs [6–8,12,17]. However, accurate modeling of the electronic properties of TMDCs is not trivial: Owing to the presence

of spin-orbit (SO) coupling [7], full spinorial Kohn-Sham wave functions are required to describe the energy splitting of the highest occupied band at the high-symmetry point *K* of the first Brillouin zone. In addition, the optical properties of the ML-TMDCs are subject to strong excitonic effects, the interactions between electron-hole pairs, and therefore require computation in an appropriate theoretical framework [12,17]. Typically, electron-hole interactions are included within the many-body perturbation theory (MBPT) formalism via solution of the computationally demanding Bethe-Salpeter equation (BSE) [26,27]. These two methodological complexities are of paramount importance for simulations of TMDCs since it is this combination of SO coupling and excitonic effects that gives rise to the characteristic peak multiplicities observed in optical absorption spectra.

In spite of these simulation requirements, continued improvements to hardware and software resources in recent years have facilitated more routine simulations of the optical properties of different TMDCs. Ramasubramaniam computed the imaginary components of the dielectric function at the GW-BSE level for a range of Mo- and W-dichalcogenide monolayers [17]. Subsequently, the imaginary part of the dielectric function of ML-MoS<sub>2</sub> has been reported on numerous occasions, for instance by Qiu *et al.* [10,11], Molina-Sanchez *et al.* [12,14], and Palummo *et al.* [28]. The simulation of the imaginary part of the dielectric function for other TMDC MLs is also widely reported on, the works of Berkelbach *et al.* [29], Bernardi *et al.* [30], and Palummo *et al.* [28] provide just a few instances for MoS<sub>2</sub>, MoSe<sub>2</sub>, WS<sub>2</sub>, and WSe<sub>2</sub> monolayers. Critically, each of these examples

\*joshua.elliott@manchester.ac.uk

†zhemi.xu@unipd.it

include spin-orbit coupling and excitonic relaxation in their simulations.

Yet, this interest has so far overlooked other TMDC optical properties, where features are not related to the absorption spectrum. To highlight this point, consider that basic, yet extremely sensitive, optical techniques, such as ellipsometry, can be applied in order to provide experimental access to the surface conductivity ( $\sigma$ ) and surface susceptibility ( $\chi$ ) [31,32]. The  $\sigma$  is proportional to the imaginary part of the dielectric function and has been well simulated. Little attention has been given to the simulation of  $\chi$ , which is proportional to the real part of the dielectric function and requires additional convergence testing. Recently, Despoja *et al.* [15] and Rukelj *et al.* [16] computed the real part of the dielectric function for ML-MoS<sub>2</sub>, but in both of these contributions simulations were carried out without excitonic effects. Only very recently, in a theoretical investigation of the in- and out-of-plane optical conductivities, Guilhon *et al.* computed the real and imaginary components of the 2D optical conductivity for several single layer materials, which included ML-MoS<sub>2</sub> [33]. These simulations have been carried out both at the independent (quasi)particle and *GW*-BSE levels of theory, and reinforce the importance of excitonic effects in the description of both the real and imaginary components of the in-plane conductivity for MoS<sub>2</sub> [33].

In this work, we continue to fill this knowledge gap by coupling theoretical simulations and experimental measurements to obtain the  $\sigma$  and  $\chi$  for ML-MoS<sub>2</sub> and for ML-WSe<sub>2</sub>. The combination of the BSE-level simulations and experimental ellipsometric measurements have facilitated the identification of several secondary peaks associated with excitonic series in our spectra. The paper is organized as follows, In Sec. II we describe our approaches for computing 2D optical quantities from the excitonic dielectric function and our experimental synthesis and measurements of the samples. In Sec. III we evaluate the convergence of the real and imaginary parts of the dielectric function that are used to build the 2D in-plane conductivity and discuss the extent to which the results of our simulations are in agreement with our experimental measurements.

## II. METHODS

### A. Computational details

In the first step of our procedure, we have used density functional theory (DFT) as implemented in PW.X code of the QUANTUM ESPRESSO distribution [34,35]. The geometrical parameters used in our calculations are summarized in Table I; lattice constants  $a$  and interion distances  $d_{MX}$  were taken from previous theoretical works [10,11,29]. Kohn-Sham wave

TABLE I. The geometric parameters  $a$  and  $d_{MX}$  (in Å) used in our DFT simulations. The converged parameters used in the BSE simulations of Mo<sub>2</sub> and WSe<sub>2</sub>.

	$a$	$d_{MX}$	<b>k</b> -grid	t-space	<b>G</b> -vectors	Empty states
MoS <sub>2</sub>	3.15	1.57	24 × 24	10	8 Ry	200
WSe <sub>2</sub>	3.29	1.67	24 × 24	10	8 Ry	200

functions, computed within the local density approximation (LDA), have been expanded in a basis of plane waves with an energy cutoff of 60 Ry (816 eV). The atomic cores were treated using fully-relativistic norm-conserving pseudopotentials including the Mo semicore  $4s$ ,  $4p$ , and  $4d$  states and W semicore  $5s$ ,  $5p$ , and  $5d$  states in the valence band.

For the calculation of the band structure and excitonic dielectric function we use the  $G_0W_0$  approximation and Bethe-Salpeter equation, respectively; these have been implemented in the YAMBO code [36,37]. To remove any spurious electrostatic interactions between periodically replicated images an interlayer spacing  $L$  (vacuum separation) of 25.2 Å has been employed and the Coulomb interaction has been truncated at a distance of 21 Å according to the scheme of Rozzi *et al.* [38]. In the computation of  $\varepsilon(\omega)$  we apply scissor operators to match the quasiparticle gaps [39,40] (including emergent zero-point vibrational effects observed in the solution of the temperature-dependent BSE for MoS<sub>2</sub> [14]) and apply stretching factors of 1.2 (1.4) to the valence and conduction band energies for MoS<sub>2</sub> (WSe<sub>2</sub>). The *GW* and BSE calculation parameters required for these calculations are reported in Table I. In order to match experimental resolution a broadening of 60 meV is applied to the computed  $\chi$  and  $\sigma$ .

### B. Surface conductivity and susceptibility from first principles

The purpose of this section is twofold, first to demonstrate how to relate the surface conductivity and susceptibility to the in-plane components of the dielectric tensor and second, how these components can be computed from many-body perturbation theory. The same concepts have been previously introduced in order to obtain both the in-plane and out-of-plane 2D optical conductivities of several 2D materials, including MoS<sub>2</sub>, from first principles [33,41,42].

We start from the tensor-vector form of Ohm's law, which relates the frequency-dependent current density,  $\mathbf{J}$  to the electric field,  $\mathbf{E}$ , via the rank-2 complex conductivity tensor  $\boldsymbol{\sigma}$ . Using Einstein summation conventions, this is expressed element wise as

$$J_i(\omega) = \sigma_{ij}(\omega)E_j(\omega) \quad (1)$$

where, in Cartesian coordinates, the indices  $i$  and  $j$  run over the  $x$ ,  $y$ , and  $z$  axes. The tensor  $\boldsymbol{\sigma}$  completely defines the state of the conductivity of a material, making it equally applicable to isotropic and anisotropic media. In particular, two-dimensional materials are an example of an anisotropic system: Assuming that the crystal is oriented in the  $xy$  plane, the macroscopic polarization along the  $z$  direction (orthogonal to the sheet) is assumed to be zero. In this case the conductivity tensor has the form

$$\boldsymbol{\sigma}(\omega) = \begin{bmatrix} \sigma_{xx}^{\parallel} & \sigma_{xy}^{\parallel} & 0 \\ \sigma_{yx}^{\parallel} & \sigma_{yy}^{\parallel} & 0 \\ 0 & 0 & 0 \end{bmatrix}. \quad (2)$$

In other words, only the in-plane components parallel to the sheet contribute to the conductivity, such that  $\sigma_{ij}^{\parallel}$  are nonzero when  $i$  and  $j$  are  $x$  or  $y$ , and  $\sigma_{ij}^{\perp} = 0$  if  $i$  or  $j = z$ . Such an approximation has recently been validated by the fact that the simulated contributions due to out-of plane polarizations can

be up to a factor of 1000 smaller than in-plane ones for these types of system [33].

We consider systems that are isotropic in the two-dimensional crystal plane, which means that off-diagonal elements of  $\sigma$  are also zero. Thus, the description of the conductivity can be further reduced such that we can adopt the notation  $\sigma^{\parallel} = \sigma_{xx}^{\parallel}$ . The complex  $\sigma^{\parallel}$  conveniently provides access to the surface conductivity  $\sigma$  and susceptibility  $\chi$ . The surface conductivity is obtained from the real part of the in-plane conductivity

$$\sigma = \text{Re } \sigma^{\parallel}(\omega) \quad (3)$$

which is analogous to the 2D optical conductivity that was very recently reported for MoS<sub>2</sub> by Guilhon *et al.* [33]. On the other hand, the surface susceptibility instead is derived from the imaginary components of the conductivity,

$$\chi = \frac{\lambda}{2\pi c \epsilon_0} \text{Im } \sigma^{\parallel}(\omega) \quad (4)$$

where  $\lambda$  is the wavelength associated with incoming radiation and  $c$  and  $\epsilon_0$  are constants corresponding to the speed of light in vacuum and the vacuum permittivity. What remains is to establish a pathway to compute  $\sigma^{\parallel}$  from first-principles simulations.

The macroscopic dielectric tensor  $\epsilon$  is computed from linear-response based electronic structure approaches (as described below) and can be linked to the conductivity through equation (1) and the Maxwell-Ampère relation [31]

$$\sigma^{\parallel}(\omega) = -i\epsilon_0\omega[\epsilon^{\parallel}(\omega) - 1]. \quad (5)$$

It should be noted that here we have introduced the in-plane dielectric function  $\epsilon^{\parallel}$ . Through similar considerations to the conductivity, it can be shown that  $\epsilon^{\parallel} = \epsilon_{xx}$  is the only relevant element of  $\epsilon$  for a two-dimensional sheet with in-plane isotropy.

In the simulations presented in this work electronic wave functions are expanded on a basis set consisting of plane waves, thereby enforcing a requirement for the use of periodic boundary conditions (PBCs). The resulting two-dimensional models actually describe an artificial crystal structure with an interlayer spacing  $L$  along the axis parallel to the surface normal. Therefore, the computed  $\epsilon^{\parallel}$  and  $\sigma^{\parallel}$  are actually superlattice quantities [41], even in the limit of large  $L$  where interactions between periodic images are negligible, these will be denoted with a subscript SL. As we are concerned with the two-dimensional response to the in-plane electric field we utilize a simple relationship which translates the three-dimensional SL in-plane conductivities to two dimensions [15,41–43]

$$\sigma_{2D}^{\parallel}(\omega) = L \sigma_{SL}^{\parallel}(\omega). \quad (6)$$

This is equivalent to treating the atomically thin sheets as intrinsically two-dimensional objects [15]. Concerning the units, equation (6) transforms the dimensions from per unit volume to per unit area. Thus  $\sigma_{2D}^{\parallel}(\omega)$  may be directly obtained from the  $\epsilon_{SL}^{\parallel}(\omega)$  by substituting equation (6) into (5):

$$\sigma_{2D}^{\parallel}(\omega) = -i\epsilon_0\omega L [\epsilon_{SL}^{\parallel}(\omega) - 1]. \quad (7)$$

To compute the complex dielectric tensor within the many-body perturbation theory formalism, we start from the Bethe-Salpeter equation. Within the Tamm-Dancoff approximation [27] and cast in the transition space of the electron-hole pairs, this amounts to solving a two-particle Schrödinger-like eigenvalue problem

$$\sum_{v'c'} H_{vc}^{2p} A_{v'c'k'}^{\lambda} = E^{\lambda} A_{vc\mathbf{k}}^{\lambda}(\mathbf{r}) \quad (8)$$

where the indices  $v$  and  $c$  denote states in the valence and conduction manifold and  $E^{\lambda}$  is the energy associated with some vertical transition eigenstate  $A^{\lambda}$ . Electron-hole interactions enter into the two-particle Hamiltonian like operator

$$H_{v'c'k'}^{2p} = (\epsilon_{c\mathbf{k}} - \epsilon_{v\mathbf{k}}) \delta_{vv'} \delta_{cc'} \delta_{\mathbf{k}\mathbf{k}'} + (f_{v\mathbf{k}} - f_{c\mathbf{k}}) [2V_{vc}^{v'c'k'} - W_{vc}^{v'c'k'}] \quad (9)$$

which is the sum of a diagonal—noninteracting—term plus an electron-hole exchange,  $V_{vc}^{v'c'k'}$ , and screened electron-hole Coulomb interaction  $W_{vc}^{v'c'k'}$ , term. These two additional two-particle terms account for local-field effects, which arise from the redistribution of charge densities brought about through the interaction with light, the mixing of single-particle transitions, the renormalization of excitation energies and formation of excitonic states with subband gap energies.

In the optical limit, i.e., where  $\mathbf{q} \rightarrow 0$ , the macroscopic dielectric tensor can be obtained from the microscopic dielectric tensor or density-density response tensor,

$$\epsilon_{SL} = \lim_{\mathbf{q} \rightarrow 0} [\epsilon(\mathbf{q})^{-1}]_{\mathbf{G}=0, \mathbf{G}'=0}^{-1} = 1 - v(\mathbf{q}) \chi_{\mathbf{G}=0, \mathbf{G}'=0} \quad (10)$$

where  $\mathbf{q}$  is a vector in the first Brillouin zone and  $\mathbf{G}$  is a reciprocal lattice vector. Expressed in terms of single-particle Kohn-Sham states and the eigenstates of equation (8), this is

$$\epsilon_{SL}^{\parallel}(\omega) = 1 - \lim_{\mathbf{q} \rightarrow 0} \frac{8\pi}{|\mathbf{q}|^2 \Omega N_q} \sum_{\lambda} \left| \sum_{vc} A_{cv\mathbf{k}}^{\lambda} \frac{\rho_{vc\mathbf{k}}}{\omega - E_{\lambda}} \right| \quad (11)$$

where  $\rho$  is the dipole matrix element  $\langle c\mathbf{k} | e^{i(\mathbf{q}+\mathbf{G})\cdot\mathbf{r}} | v\mathbf{k} \rangle$  associated with a given vertical excitation. Given that our focus is on computing the in-plane elements of the conductivity tensor, we limit our considerations to dipole moments oriented in the plane of the TMDC. Finally, this means that the surface conductivity and susceptibility can be computed from BSE simulations by inserting the computed  $\epsilon_{SL}^{\parallel}$  in to equation (7).

### C. Experimental measurements

The large-area, continuous monolayer MoS<sub>2</sub> and WSe<sub>2</sub> were grown by chemical vapor deposition (CVD) on SiO<sub>2</sub>/Si substrates. Then, the films were transferred, respectively, on a BK7 substrate and on a sapphire substrate for spectroscopic ellipsometry measurements. The ellipsometric measurements were operated in ambient conditions at room temperature by a VASE ellipsometer (J. A. Wollam). The measured spectral range is 400–900 nm, which encompasses the entire visible range of light. The backside of the substrate was taped to avoid backside reflections. The experimental reproducibility is ensured by measuring various positions and incoming beams with different incidence angles.

### III. RESULTS AND DISCUSSION

#### A. Monolayer TMDC band structures

Strong enhancements in the photoluminescence of monolayer TMDCs with respect to bulk are an experimental indication of a transition from an indirect to direct band gap. This change in behavior is well understood: The indirect gap, which has a lower energy in the bulk limit, is opened as the materials thickness is decreased, [5] while the direct gap remains constant. Each of the monolayer TMDCs MoS<sub>2</sub>, WS<sub>2</sub>, MoSe<sub>2</sub>, and WSe<sub>2</sub> was thought to have a direct gap [44,45], yet more recent scanning tunneling spectroscopy and photoluminescence measurements suggest WSe<sub>2</sub> maintains an indirect gap in the monolayer limit [39,40]. Here we focus on monolayer MoS<sub>2</sub> and WSe<sub>2</sub>; we use first-principles calculations based on DFT and the *GW* approximation to compute their band structures. On top of the experimental findings described above, it has been established in previous theoretical investigations that monolayer MoS<sub>2</sub> has a direct gap (the interested reader is directed to Refs. [8,10,17,29,46] where the band structure is reported.) On the other hand, over the course of the last several years, both direct [7,8,28,47] and indirect [17,40] band structures have been computed for WSe<sub>2</sub>. In light of the conflicting experimental and theoretical results, it is informative to present the WSe<sub>2</sub> band structure computed at the LDA and  $G_0W_0$  level; the results are plotted in Fig. 1.

Our simulations yield a lower energy indirect gap between the high symmetry point *K* at the top of the valence band and the midpoint between  $\Gamma$  and *K* (marked with a vertical dashed line in Fig. 1) at the bottom of the conduction band, and a higher-energy direct gap at *K*. In comparison with the experimental values (2.1 and 2.2 eV [39]), as is typically the case for semiconducting materials, the LDA (gray, Fig. 1) indirect and direct gaps are underestimated by 0.8 eV and 0.7 eV, respectively. It is worthwhile to point out that, despite overestimating the energy gap, the LDA indirect-direct gap energy difference (90 meV) is in very good agreement with experiment. While the LDA calculations do not provide quantitative agreement with experimental measurements, our computed WSe<sub>2</sub> electronic structure is comparable to the

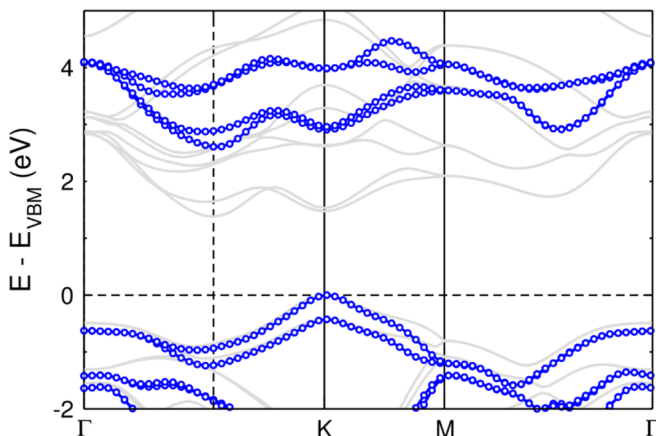


FIG. 1. The computed LDA (gray) and  $G_0W_0$  (blue, circles) band structure for the WSe<sub>2</sub> monolayer.

GGA-level band structure reported by Hsu *et al.* [40]. The GGA indirect and direct energy gaps are approximately 1.3 and 1.4 eV, respectively, just 0.1 eV smaller than what we find here.

The quasiparticle band structure, computed perturbatively as  $G_0W_0$  corrections to the LDA values, is also plotted with blue circles in Fig. 1. In our simulations, the quasiparticle corrections reduce the error in the indirect gap, which is overestimated by 0.5 eV with respect to experiment. Our  $G_0W_0$  simulations also overestimate the direct gap by 0.8 eV, most likely due to the LDA starting point. Better agreement with the experimental energy gaps can be obtained by computing the quasiparticle corrections on top of hybrid wave functions. For instance, Ramasubramaniam computed an indirect band structure starting from HSE eigenvalues and eigenstates [17], overestimating the experimental results by 0.2 eV. Yet, despite the difference in the energy gaps, the main features of the LDA and  $G_0W_0$  band structure remain unchanged: The indirect gap between the valence band maximum at *K* and the midpoint between *K* and  $\Gamma$  is smaller than the direct gap at *K* and the spin-orbit interaction splits the top of the valence band by 0.4 eV (vs 0.5 eV at HSE +  $G_0W_0$  level).

Since the quasiparticle eigenstates and eigenspectrum act as the starting point for the computation of the dielectric function in BSE simulations, we could in principle improve the quality of our BSE simulations by changing the DFT exchange-correlation potential. Yet, since our LDA + SOC electronic structure is in qualitative agreement both with the GGA and hybrid band structures, we can avoid these more time-consuming simulations by instead applying a scissor operator directly onto the DFT eigenspectrum, in the same way that MoS<sub>2</sub> is often treated at this level of theory [12,13].

#### B. Calculation of $\epsilon$

For both monolayer MoS<sub>2</sub> and WSe<sub>2</sub>, through investigation of their optical absorption properties, the imaginary parts of the dielectric function have already been widely reported on [10–12,14,17,29,30]. This interest has been driven by the TMDC-monolayer optical absorption in the visible part of the electromagnetic spectrum, which has practical relevance in, for example, phototransistor technology. Instead, the real parts,  $\epsilon_1$ , which can provide further comparison with experimental measurements through properties such as the surface susceptibility, have received almost no attention from the theoretical community [16]. As a consequence, it is important for us to ensure that the level convergence of  $\epsilon_1$  matches that of  $\epsilon_2$ . Owing to the volume of computationally demanding simulations required, and to expedite our progress, we carried out exhaustive convergence testing for MoS<sub>2</sub> and rely on the transferability of those parameters to inform our convergence testing for the simulations of WSe<sub>2</sub>.

Convergence criterion are obtained via the inspection of equation (11), the sums over single particle states and  $\mathbf{k}$  points indicate that the assessment of the convergence of  $\epsilon_1$  should consider the integration of the first Brillouin zone (BZ) and the transition space in which excitations occur as well as the total number of  $\mathbf{G}$  vectors and the number of empty states used to build the description of the polarizability. In our case, the convergence of both  $\epsilon_1$  and  $\epsilon_2$  with respect



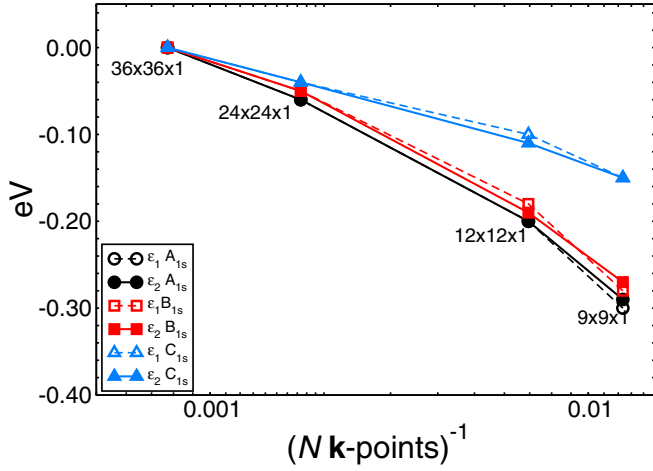


FIG. 2. A plot of the  $\mathbf{k}$ -point convergence for the  $A_{1s}$ ,  $B_{1s}$ , and  $C_{1s}$  peaks in the computed real and imaginary parts of the  $\text{MoS}_2$  dielectric function  $\varepsilon_1$  and  $\varepsilon_2$ .

to the calculation parameters was most sensitive to (i) the  $\mathbf{k}$ -point sampling of the BZ and (ii) to the number of bands that were considered when building the excitonic Hamiltonian in the single-particle transition space. The behavior of the monolayer  $\text{MoS}_2$  superlattice dielectric function with respect to these parameters is plotted in Figs. 2 and 3.

Assessing first the  $\mathbf{k}$ -point convergence, we plot in Fig. 2 the change in the relative energies of the main adsorption peaks ( $A_{1s}$ ,  $B_{1s}$ , and  $C_{1s}$ ) as a function of increasing  $\mathbf{k}$ -point densities, each peak is normalized to the highest density  $36 \times 36 \times 1$  grid. It can be seen that both the  $\varepsilon_1$  and  $\varepsilon_2$  exhibit similar behavior with increasing  $\mathbf{k}$ -point meshes. Both reach an acceptable (0.1 eV) level of convergence in all three adsorption peaks for a  $24 \times 24 \times 1$  grid, with the excitonic  $A_{1s}$  and  $B_{1s}$  signals more sensitive to BZ sampling. We note that higher levels of convergence are achievable for significantly higher  $\mathbf{k}$ -point meshes [10–12], however we deemed this

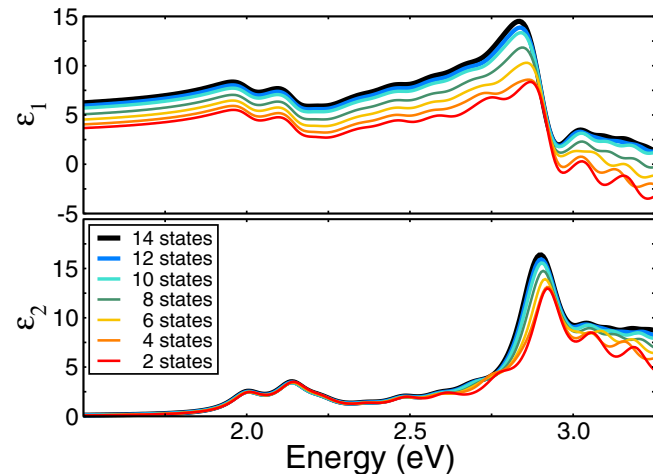


FIG. 3. The convergence of the real and imaginary parts of the  $\text{MoS}_2$  dielectric function  $\varepsilon_1$  and  $\varepsilon_2$  as a function of the number of single particle states used to build the excitonic Hamiltonian.

TABLE II. Comparison of the peak positions in the  $\text{MoS}_2$  and  $\text{WSe}_2$  experimental (computed)  $\chi$  and  $\sigma$ . All values are reported in nm.

Peak	$\text{MoS}_2$				$\text{WSe}_2$			
	$\chi$		$\sigma$		$\chi$		$\sigma$	
$A_{1s}$	680	(694)	664	(673)	770	(809)	751	(772)
$A_{2s}$	—	(—)	—	(—)	705	(706)	681	(688)
$B_{1s}$	623	(639)	611	(620)	625	(605)	602	(581)
$B_{2s}$	563	(555)	550	(545)	—	(—)	—	(—)
$B_{3s}$	—	(524)	—	(520)	—	(—)	—	(—)
$C_{1s}$	445	(463)	429	(451)	525	(523)	508	(506)
$C_{2s}$	—	(—)	—	(—)	—	(469)	—	(460)
D	—	(—)	—	(—)	442	(432)	426	(416)

level of convergence to be the most suitable tradeoff between accuracy and computational viability.

For the convergence of the second parameter, the number of single particle states used to build the excitonic Hamiltonian, the  $\varepsilon_1$  and  $\varepsilon_2$  are plotted in the two panels of Fig. 3. We increase the number of valence and conduction states linearly and symmetrically about the HOMO-LUMO gap such that an excitonic Hamiltonian with eight states is comprised of four filled and four empty states. As the number of states increases, both the intensity and energy of the peaks have to be taken into consideration. While in the case of  $\mathbf{k}$ -point sampling convergence of  $\varepsilon_1$  and  $\varepsilon_2$  occurs at the same interval, we note that the  $\varepsilon_1$  requires considerably more single particle transitions in order to reach convergence than  $\varepsilon_2(\omega)$ , even at low energies. The excitonic peaks in the imaginary part of the spectrum are converged for a transition space which includes four states spanning the HOMO-1  $\rightarrow$  LUMO + 1, yet to reach satisfactory convergence of the real part, a range spanning 10 states is required. The final set of parameters used for our calculations of  $\chi$  and  $\sigma$  is reported in Table I.

### C. Comparison of computed and measured $\chi$ and $\sigma$

Our BSE calculations of  $\text{Re } \varepsilon_{\text{SL}}(\omega)$  and  $\text{Im } \varepsilon_{\text{SL}}(\omega)$ , provide access to the theoretical surface susceptibility  $\chi$  and surface conductivity  $\sigma$  using equation (7). The experimental  $\chi$  and  $\sigma$  were obtained from the ellipsometric parameter  $\Psi$  and  $\Delta$  using the surface current (SC) model [32]. The calculated and experimentally derived  $\chi$  and  $\sigma$  of  $\text{MoS}_2$  and  $\text{WSe}_2$  are presented in Figs. 4 and 5, and the analysis of the spectral features is presented in Table II.

In Fig. 4 we plot the computed and measured  $\chi$  (a) and  $\sigma$  (b) for  $\text{MoS}_2$ , where three strong peaks are observed. By convention these are labeled as A, B, and C [31], with the A and B peaks arising from direct transitions between the the highest energy valence- and lowest energy conduction bands at the K point in the Brillouin zone [31,48–50], and the C peak from six nearly degenerate exciton states comprising transitions between the highest valence band and the first three conduction bands (near, but not directly at  $\Gamma$ ) [10,31,51]. The valence band splitting, which gives rise to the energetic separation of the A and B peaks, is caused by SO interactions that are fully accounted for by our computational method

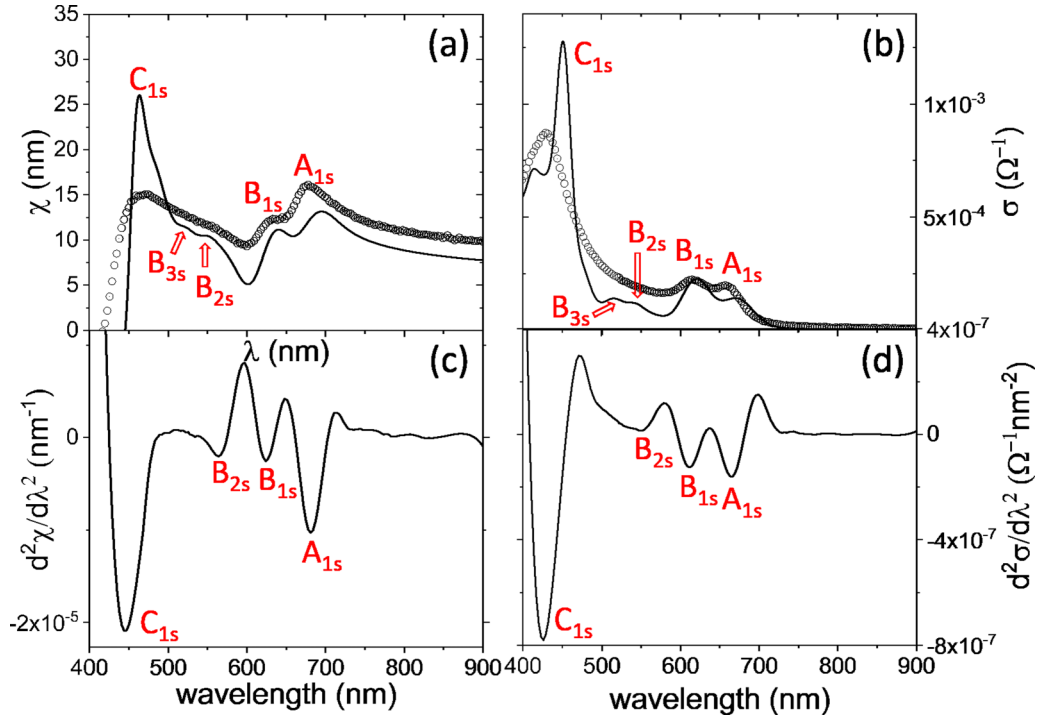


FIG. 4. A comparison of the surface susceptibilities and optical conductivities for monolayer MoS<sub>2</sub> (a), (b) and the second derivative of the experimental results (c), (d). In (a) and (b), theoretical data is reported with solid lines and experimental data is reported with hollow circles.

[12,34–36]. A detailed analysis of the main peak positions is provided in Table II.

In addition to the main peaks, our calculated spectra show other features that are not immediately evident in the ellipsometric data. These are the excited excitonic states, marked

as B<sub>2s</sub> and B<sub>3s</sub>. These peaks were not observed in previously reported ellipsometric data analysis of single-layer MoS<sub>2</sub> [52–59], but they have been identified in photoluminescence excitation spectroscopy [48]. We have been able to extract the B<sub>2s</sub> peak from ellipsometry measurements by numerically

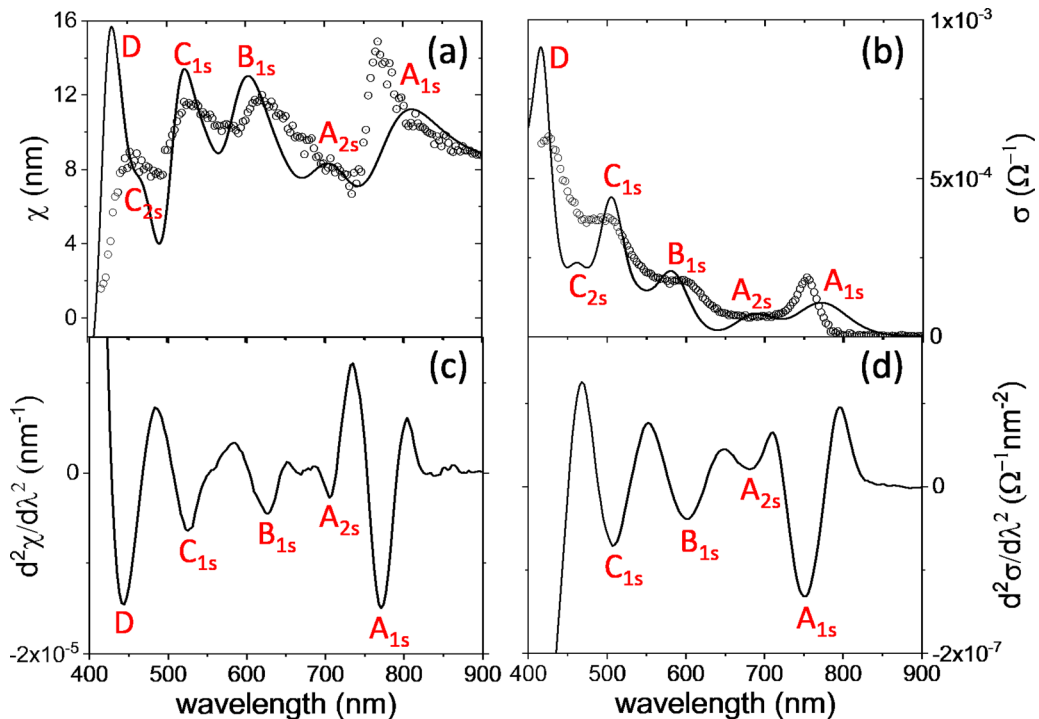


FIG. 5. A comparison of the surface susceptibilities and optical conductivities for monolayer WSe<sub>2</sub> (a), (b) and the second derivative of the experimental results (c), (d). In (a) and (b), theoretical data is reported with solid lines and experimental data is reported with hollow circles.

TABLE III. Energies (E) and energy spacing ( $\Delta$ ) between the ground states and excited states of MoS<sub>2</sub> and WSe<sub>2</sub>. Data are extracted from the  $\chi$  spectra. All values are reported in eV.

Peak	MoS <sub>2</sub>				WSe <sub>2</sub>			
	Exp.		Cal.		Exp.		Cal.	
	E	$\Delta$	E	$\Delta$	E	$\Delta$	E	$\Delta$
A <sub>1s</sub>	1.82		1.79		1.61		1.53	
A <sub>2s</sub>	–	(–)	–	(–)	1.76	(0.15)	1.76	(0.23)
B <sub>1s</sub>	1.99		1.94		1.98		2.05	
B <sub>2s</sub>	2.20	(0.21)	2.23	(0.29)	–	(–)	–	(–)
B <sub>3s</sub>	–	(–)	2.37	(0.43)	–	(–)	–	(–)
C <sub>1s</sub>	2.79		2.68		2.36		2.37	
C <sub>2s</sub>	–	(–)	–	(–)	–	(–)	2.64	(0.27)

calculating the second derivatives. The experimental data was first smoothed using Savitzky Golay method as implemented in Origin® [60,61] and then taking numerical derivatives, which are plotted in Figs. 4(c) and 4(d). The second derivatives analysis reveals the excited exciton peaks in both  $\chi$  and  $\sigma$ . These measured and computed excited exciton peaks are reported in Table II and in Table III. The overall agreement in between the theoretical and experimental results is very good.

The  $\chi$  and  $\sigma$  spectra of monolayer WSe<sub>2</sub> are shown in the left and right panels of Fig. 5, respectively. As in the case of MoS<sub>2</sub>, peaks A and B are direct transitions at the K point [60]. The features labeled as C and D peaks have been proposed as interband transitions mostly occurring near the  $\Gamma$  point [31,62]. The A<sub>2s</sub> excited exciton state was previously observed via photoluminescence spectroscopy [60] observed in both our calculated  $\chi$  and  $\sigma$ . Again we need to apply the second derivatives analysis to our experimental spectra to elucidate this excited excitonic state [in Figs. 5(c) and 5(d)].

#### IV. CONCLUSIONS

We have used a recent formulation for two-dimensional optical properties from first principles simulations in order to investigate  $\chi$  and  $\sigma$  in monolayer-MoS<sub>2</sub> and -WSe<sub>2</sub> via BSE calculations. While the convergence of the imaginary

part of the dielectric function, from which we obtain  $\sigma$ , has been reported several time in literature for these materials, here the convergence of the real part has been tested with this computational method (and used to compute  $\chi$ ). This convergence has been carried out in an exhaustive way for the case of the single-layer MoS<sub>2</sub>, which we then used to inform our testing for WSe<sub>2</sub>.

The importance of computing both  $\chi$  and  $\sigma$  comes from the fact that both of these quantities are directly accessible experimentally through ellipsometry. A convincing proof of good computational convergence is indirectly provided by the comparison with the experimental data reported here: They fit equally well the computed  $\chi$  and  $\sigma$ .

The main features (A, B, C, D peaks) of the computed spectra are clearly resolved also in ellipsometry measurements, while theoretically we also observe the emergence peaks that can be attributed to excited exciton states. These additional A<sub>2s</sub>, B<sub>2s</sub>, B<sub>3s</sub>, and C<sub>2s</sub> peaks align very well with previous results for MoS<sub>2</sub> and WSe<sub>2</sub>. The peak B<sub>2s</sub> for MoS<sub>2</sub> and A<sub>2s</sub> for WSe<sub>2</sub> features in our measured spectra once the second derivative of the experimental  $\chi$  and  $\sigma$  is performed. These excited states are observed in ellipsometric measurements at ambient conditions, thus, these results demonstrate once more the importance of merging computational and experimental methods to characterize the optical response of 2D crystals as well as highlighting the high degree of precision that ellipsometry can reach in measuring both  $\chi$  and  $\sigma$ .

#### ACKNOWLEDGMENTS

J.E. and P.U. acknowledge funding from the EU-H2020 research and innovation programme under Grant agreement No. 654360 NFFA-Europe and acknowledge PRACE (project ID 20171633963) for awarding access to Marconi at CINECA, Italy. M.Me. and Z.X. acknowledge financial support from Dipartimento di Fisica e Astronomia G. Galilei, Università Degli Studi di Padova, funding BIRD170839/17. The computing resources and the related technical support used for this work have been provided by CRESCO/ENEAGRID High Performance Computing infrastructure and its staff. CRESCO/ENEAGRID High Performance Computing infrastructure is funded by ENEA, the Italian National Agency for

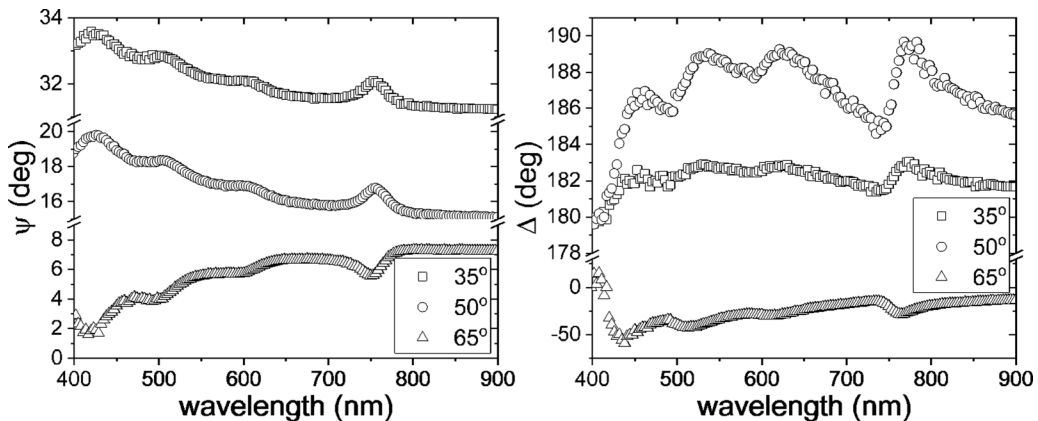


FIG. 6. Experimental ellipsometric parameter  $\Psi$  and  $\Delta$  for the single-layer WSe<sub>2</sub>.

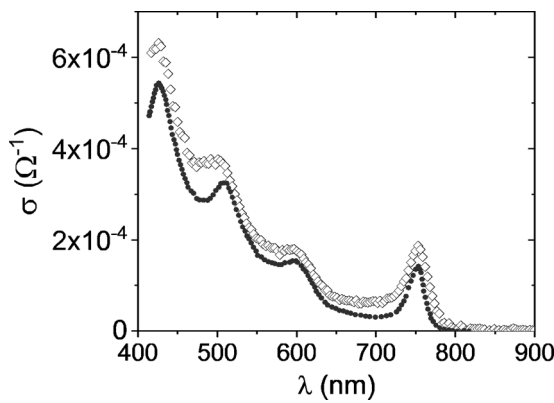


FIG. 7. Our single-layer WSe<sub>2</sub> (hollow dots) versus the one reported in Ref. [31] (solid dots).

New Technologies, Energy and Sustainable Economic Development and by Italian and European research programmes, see <http://www.cresco.enea.it/english> for information.

The idea for the work was originally conceived in discussions between M.Me. and P.U. Simulations and their analysis

were carried out by M.Ma. and J.E.; G.J. and M.C. prepared the samples under the supervision of X.Z. and measurements and data analysis were done by Z.X., M.Me., and A.M. J.E. and Z.X. prepared the original draft; all authors have been involved in the expansion of the manuscript and have approved the final version.

## APPENDIX

The ellipsometric parameter  $\Psi$  and  $\Delta$  of the single-layer WSe<sub>2</sub> on sapphire are provided in Fig. 6. The  $\Psi$  and  $\Delta$  spectra of the MoS<sub>2</sub> can be found in our previous publication [52]. We observe that the  $\Psi$  decreases with the wavelength for angles of incidence smaller than the Brewster's angle ( $\theta_B$ ) and increases above  $\theta_B$ . The  $\Delta$  of WSe<sub>2</sub> stays around  $0^\circ$  above  $\theta_B$ , while varies around  $180^\circ$  below  $\theta_B$ . Peaks contributed by excitonic states are also observed in both spectra of  $\Psi$  and  $\Delta$ .

In Fig. 7, the extracted  $\sigma$  of WSe<sub>2</sub> is compared to the reported surface conductivity from Ref. [31]. This comparison confirms that we are dealing with a good quality single-layer crystal.

- [1] Q. H. Wang, K. Kalantar-Zadeh, A. Kis, J. N. Coleman, and M. S. Strano, *Nat. Nanotechnol.* **7**, 699 (2012).
- [2] D. Jariwala, V. K. Sangwan, L. J. Lauhon, T. J. Marks, and M. C. Hersam, *ACS Nano* **8**, 1102 (2014).
- [3] S. Manzeli, D. Ovchinnikov, D. Pasquier, O. V. Yazyev, and A. Kis, *Nat. Rev. Mater.* **2**, 17033 (2017).
- [4] Y.-H. Wang, K.-J. Huang, and X. Wu, *Biosens. Bioelectron.* **97**, 305 (2017).
- [5] K. F. Mak, C. Lee, J. Hone, J. Shan, and T. F. Heinz, *Phys. Rev. Lett.* **105**, 136805 (2010).
- [6] A. Splendiani, L. Sun, Y. Zhang, T. Li, J. Kim, C.-Y. Chim, G. Galli, and F. Wang, *Nano Lett.* **10**, 1271 (2010).
- [7] Z. Y. Zhu, Y. C. Cheng, and U. Schwingenschlöggl, *Phys. Rev. B* **84**, 153402 (2011).
- [8] A. Kumar and P. K. Ahluwalia, *Eur. Phys. J. B* **85**, 186 (2012).
- [9] K. F. Mak, K. He, C. Lee, G. H. Lee, J. Hone, T. F. Heinz, and J. Shan, *Nat. Mater.* **12**, 207 (2013).
- [10] D. Y. Qiu, F. H. da Jornada, and S. G. Louie, *Phys. Rev. Lett.* **111**, 216805 (2013).
- [11] D. Y. Qiu, F. H. da Jornada, and S. G. Louie, *Phys. Rev. Lett.* **115**, 119901(E) (2015).
- [12] A. Molina-Sánchez, D. Sangalli, K. Hummer, A. Marini, and L. Wirtz, *Phys. Rev. B* **88**, 045412 (2013).
- [13] A. Molina-Sánchez, K. Hummer, and L. Wirtz, *Surf. Sci. Rep.* **70**, 554 (2015).
- [14] A. Molina-Sánchez, M. Palummo, A. Marini, and L. Wirtz, *Phys. Rev. B* **93**, 155435 (2016).
- [15] V. Despoja, Z. Rukelj, and L. Marušić, *Phys. Rev. B* **94**, 165446 (2016).
- [16] Z. Rukelj, A. Štrkalj, and V. Despoja, *Phys. Rev. B* **94**, 115428 (2016).
- [17] A. Ramasubramaniam, *Phys. Rev. B* **86**, 115409 (2012).
- [18] G. Plechinger, P. Nagler, J. Kraus, N. Paradiso, C. Strunk, C. Schüller, and T. Korn, *Phys. Status Solidi RRL* **9**, 457 (2015).
- [19] B. Radisavljevic, A. Radenovic, J. Brivio, V. Giacometti, and A. Kis, *Nat. Nanotechnol.* **6**, 147 (2011).
- [20] H. Fang, S. Chuang, T. C. Chang, K. Takei, T. Takahashi, and A. Javey, *Nano Lett.* **12**, 3788 (2012).
- [21] B. Radisavljevic, M. B. Whitwick, and A. Kis, *ACS Nano* **5**, 9934 (2011).
- [22] H. Wang, L. Yu, Y.-H. Lee, Y. Shi, A. Hsu, M. L. Chin, L.-J. Li, M. Dubey, J. Kong, and T. Palacios, *Nano Lett.* **12**, 4674 (2012).
- [23] Z. Yin, H. Li, H. Li, L. Jiang, Y. Shi, Y. Sun, G. Lu, Q. Zhang, X. Chen, and H. Zhang, *ACS Nano* **6**, 74 (2012).
- [24] H. S. Lee, S.-W. Min, Y.-G. Chang, M. K. Park, T. Nam, H. Kim, J. H. Kim, S. Ryu, and S. Im, *Nano Lett.* **12**, 3695 (2012).
- [25] W. Zhang, J.-K. Huang, C.-H. Chen, Y.-H. Chang, Y.-J. Cheng, and L.-J. Li, *Adv. Mater.* **25**, 3456 (2013).
- [26] G. Strinati, *La Rivista del Nuovo Cimento* **11**, 1 (1988).
- [27] G. Onida, L. Reining, and A. Rubio, *Rev. Mod. Phys.* **74**, 601 (2002).
- [28] M. Palummo, M. Bernardi, and J. C. Grossman, *Nano Lett.* **15**, 2794 (2015).
- [29] T. C. Berkelbach, M. S. Hybertsen, and D. R. Reichman, *Phys. Rev. B* **88**, 045318 (2013).
- [30] M. Bernardi, M. Palummo, and J. C. Grossman, *Nano Lett.* **13**, 3664 (2013).
- [31] Y. Li, A. Chernikov, X. Zhang, A. Rigosi, H. M. Hill, A. M. van der Zande, D. A. Chenet, E.-M. Shih, J. Hone, and T. F. Heinz, *Phys. Rev. B* **90**, 205422 (2014).
- [32] M. Merano, *Phys. Rev. A* **93**, 013832 (2016).
- [33] I. Guilhon, M. Marques, L. K. Teles, M. Palummo, O. Pulci, S. Botti, and F. Bechstedt, *Phys. Rev. B* **99**, 161201(R) (2019).
- [34] P. Giannozzi, S. Baroni, N. Bonini, M. Calandra, R. Car, C. Cavazzoni, D. Ceresoli, G. L. Chiarotti, M. Cococcioni, I. Dabo, A. Dal Corso, S. de Gironcoli, S. Fabris, G. Fratesi, R. Gebauer, U. Gerstmann, C. Gougoussis, A. Kokalj, M. Lazzeri, L. Martin-Samos, N. Marzari, F. Mauri, R. Mazzarello,



- S. Paolini, A. Pasquarello, L. Paulatto, C. Sbraccia, S. Scandolo, G. Sciauzero, A. P. Seitsonen, A. Smogunov, P. Umari, and R. M. Wentzcovitch, *J. Phys.: Condens. Matter* **21**, 395502 (2009).
- [35] P. Giannozzi, O. Andreussi, T. Brumme, O. Bunau, M. Buongiorno Nardelli, M. Calandra, R. Car, C. Cavazzoni, D. Ceresoli, M. Cococcioni, N. Colonna, I. Carnimeo, A. Dal Corso, S. de Gironcoli, P. Delugas, R. A. DiStasio, A. Ferretti, A. Floris, G. Fratesi, G. Fugallo, R. Gebauer, U. Gerstmann, F. Giustino, T. Gorni, J. Jia, M. Kawamura, H.-Y. Ko, A. Kokalj, E. Küçükbenli, M. Lazzeri, M. Marsili, N. Marzari, F. Mauri, N. L. Nguyen, H.-V. Nguyen, A. Otero-de-la Roza, L. Paulatto, S. Poncé, D. Rocca, R. Sabatini, B. Santra, M. Schlipf, A. P. Seitsonen, A. Smogunov, I. Timrov, T. Thonhauser, P. Umari, N. Vast, X. Wu, and S. Baroni, *J. Phys.: Condens. Matter* **29**, 465901 (2017).
- [36] A. Marini, C. Hogan, M. Grüning, and D. Varsano, *Comput. Phys. Commun.* **180**, 1392 (2009).
- [37] D. Sangalli, A. Ferretti, H. Miranda, C. Attaccalite, I. Marri, E. Cannuccia, P. Melo, M. Marsili, F. Paleari, A. Marrazzo, G. Prandini, P. Bonfà, M. O. Atambo, F. Affinito, M. Palumbo, A. Molina-Sánchez, C. Hogan, M. Grüning, D. Varsano, and A. Marini, *J. Phys.: Condens. Matter* **31**, 325902 (2019).
- [38] C. A. Rozzi, D. Varsano, A. Marini, E. K. U. Gross, and A. Rubio, *Phys. Rev. B* **73**, 205119 (2006).
- [39] C. Zhang, Y. Chen, A. Johnson, M.-Y. Li, L.-J. Li, P. C. Mende, R. M. Feenstra, and C.-K. Shih, *Nano Lett.* **15**, 6494 (2015).
- [40] W.-T. Hsu, L.-S. Lu, D. Wang, J.-K. Huang, M.-Y. Li, T.-R. Chang, Y.-C. Chou, Z.-Y. Juang, H.-T. Jeng, L.-J. Li, and W.-H. Chang, *Nat. Commun.* **8**, 929 (2017).
- [41] L. Matthes, O. Pulci, and F. Bechstedt, *New J. Phys.* **16**, 105007 (2014).
- [42] L. Matthes, O. Pulci, and F. Bechstedt, *Phys. Rev. B* **94**, 205408 (2016).
- [43] D. Novko, M. Šunjić, and V. Despoja, *Phys. Rev. B* **93**, 125413 (2016).
- [44] W. Zhao, Z. Ghorannevis, L. Chu, M. Toh, C. Kloc, P.-H. Tan, and G. Eda, *ACS Nano* **7**, 791 (2013).
- [45] P.-C. Yeh, W. Jin, N. Zaki, D. Zhang, J. T. Liou, J. T. Sadowski, A. Al-Mahboob, J. I. Dadap, I. P. Herman, P. Sutter, and R. M. Osgood, *Phys. Rev. B* **91**, 041407(R) (2015).
- [46] D. Liu, Y. Guo, L. Fang, and J. Robertson, *Appl. Phys. Lett.* **103**, 183113 (2013).
- [47] A. Molina-Sánchez, D. Sangalli, L. Wirtz, and A. Marini, *Nano Lett.* **17**, 4549 (2017).
- [48] H. M. Hill, A. F. Rigosi, C. Roquelet, A. Chernikov, T. C. Berkelbach, D. R. Reichman, M. S. Hybertsen, L. E. Brus, and T. F. Heinz, *Nano Lett.* **15**, 2992 (2015).
- [49] J. Wilson and A. Yoffe, *Adv. Phys.* **18**, 193 (1969).
- [50] L. F. Mattheiss, *Phys. Rev. B* **8**, 3719 (1973).
- [51] A. Carvalho, R. M. Ribeiro, and A. H. Castro Neto, *Phys. Rev. B* **88**, 115205 (2013).
- [52] G. Jayaswal, Z. Dai, X. Zhang, M. Bagnarol, A. Martucci, and M. Merano, *Opt. Lett.* **43**, 703 (2018).
- [53] S. Funke, B. Miller, E. Parzinger, P. Thiesen, A. Holleitner, and U. Wurstbauer, *J. Phys.: Condens. Matter* **28**, 385301 (2016).
- [54] V. Le, T. Kim, H. Park, H. Nguyen, X. Nguyen, and Y. Kim, *Current Appl. Phys.* **19**, 182 (2019).
- [55] B. Song, H. Gu, M. Fang, X. Chen, H. Jiang, R. Wang, T. Zhai, Y.-T. Ho, and S. Liu, *Adv. Opt. Mater.* **7**, 1801250 (2019).
- [56] H. G. Park, T. J. Kim, H. S. Kim, C. H. Yoo, N. S. Barange, V. L. Le, H. U. Kim, V. Senthilkumar, C. T. Le, Y. S. Kim *et al.*, *Appl. Spectroscopy Rev.* **51**, 621 (2016).
- [57] J. W. Park, H. S. So, S. Kim, S.-H. Choi, H. Lee, J. Lee, C. Lee, and Y. Kim, *J. Appl. Phys.* **116**, 183509 (2014).
- [58] H.-L. Liu, C.-C. Shen, S.-H. Su, C.-L. Hsu, M.-Y. Li, and L.-J. Li, *Appl. Phys. Lett.* **105**, 201905 (2014).
- [59] W. Li, A. G. Birdwell, M. Amani, R. A. Burke, X. Ling, Y.-H. Lee, X. Liang, L. Peng, C. A. Richter, J. Kong *et al.*, *Phys. Rev. B* **90**, 195434 (2014).
- [60] K. He, N. Kumar, L. Zhao, Z. Wang, K. F. Mak, H. Zhao, and J. Shan, *Phys. Rev. Lett.* **113**, 026803 (2014).
- [61] A. Savitzky and M. J. Golay, *Anal. Chem.* **36**, 1627 (1964).
- [62] A. F. Rigosi, H. M. Hill, Y. Li, A. Chernikov, and T. F. Heinz, *Nano Lett.* **15**, 5033 (2015).